Compressible flow through a porous medium: choking at pore scale and its implications

by

Jing Yuan

A Thesis Presented in Partial Fulfillment
of the Requirements for the Degree
Master of Science

Approved November 2013 by the
Graduate Supervisory Committee:

Kangping Chen, Chair
Huei-Ping Huang
Liping Wang

ARIZONA STATE UNIVERSITY

December 2013

ABSTRACT

Production from a high pressure gas well at a high production-rate encounters the risk of operating near the choking condition for a compressible flow in porous media. The unbounded gas pressure gradient near the point of choking, which is located near the wellbore, generates an effective tensile stress on the porous rock frame. This tensile stress almost always exceeds the tensile strength of the rock and it causes a tensile failure of the rock, leading to wellbore instability. In a porous rock, not all pores are choked at the same flow rate, and when just one pore is choked, the flow through the entire porous medium should be considered choked as the gas pressure gradient at the point of choking becomes singular. This thesis investigates the choking condition for compressible gas flow in a single microscopic pore. Quasi-one-dimensional analysis and axisymmetric numerical simulations of compressible gas flow in a pore scale varicose tube with a number of bumps are carried out, and the local Mach number and pressure along the tube are computed for the flow near choking condition. The effects of tube length, inlet-to-outlet pressure ratio, the number of bumps and the amplitude of the bumps on the choking condition are obtained. These critical values provide guidance for avoiding the choking condition in practice.

Key words: Compressible flow, Choked flow, Porous medium

ACKNOWLEDGMENTS

TABLE OF CONTENTS

LIST OF FIGURES

CHAPTER 1 INTRODUCTION

In recent years, increased worldwide demand for energy has pushed petroleum exploration and production to much harsher frontier areas and environments. Production wells are increasingly drilled into geologically complex formations and extended to much greater depths, some as deep as 10,000 meters below surface. High temperature and high pressure formations are frequently encountered at such depths, which present many new technological challenges. This is particular true if the formation fluid contains a compressible gas, whose *in situ* pressure can reach more than 100 MPa at 10,000 meter depth.

A highly pressurized compressible gas poses a serious threat of wellbore instability, defined as the loss of the mechanical integrity of the bore-hole, as well as gas-kick and well-blowout during drilling. It can also cause wellbore instability issues even during production for wells with open-hole completion. An open-hole completion refers to an uncased section of the producing formation (Fig. 1.1). While most completions are cased, some are open, especially in horizontal or extended reach wells where it may not be possible to cement casing efficiently. It is well documented that open-hole completions have higher productivity and greater longevity than their cased-hole counterparts (Smejkal, 1995). However, open-hole completion brings reduced wellbore stability. Even for cased completions, perforations can also experience borehole instabilities during well tests and production. Perforation instability during production is related to the phenomenon of sand production for sandstone formations (Fjaer *et al*, 2008). Unlike wellbore stability problems during drilling where the influx of the formation fluids (oil, gas) to the wellbore is intentionally prevented by the heavy drilling fluid in the wellbore,

in pre-production well tests and production such an influx of the formation fluids into the well is desired. As the reservoir fluid moves toward the wellbore, the fluid pressure decreases from the reservoir initial equilibrium pressure at the outer boundary to the well flowing pressure in the wellbore. Due to the coupling between the flow and the deformation of the fluid-saturated porous rock, this reservoir fluid pressure variation associated with the flow changes the effective stress of the formation rocks from the state of stress during drilling. This change in the formation effective stress due to the flow of the reservoir fluid can make a wellbore unstable even if it was stable during drilling operations. Such post-drilling instabilities for boreholes in wells with open-hole completions can occur for both steady flow conditions of production and unsteady flow conditions of well tests. For high pressure gas wells, post-drilling wellbore stability becomes an even more serious issue due to some peculiar properties of high pressure compressible gas flow in a porous medium discussed below.
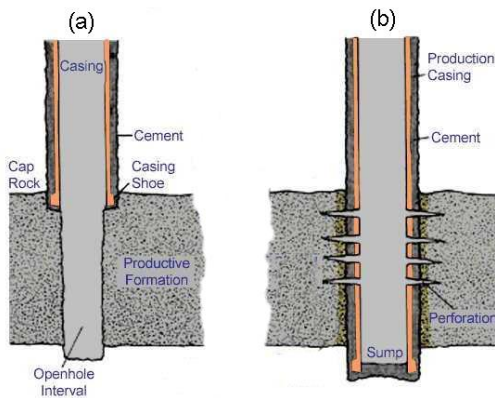
Fig. 1.1 Well completions. (a) Open-hole completion; (b) cased completion with perforations.

During production, porous media flow of the reservoir fluid in the near wellbore region plays a predominant role in determining the production-rate and the mechanical integrity of the wellbore [1-3]. In the region away from the wellbore, Darcy's law [4] prevails and the fluid pressure decreases logarithmically as the fluid moves towards the wellbore. This logarithmic pressure profile dictates that most of the pressure drop occurs near the wellbore. Additionally, the converging radial flow causes the fluid velocity to increase continuously and inertial effect becomes important in the near wellbore region. This inertial effect induces an additional pressure drop in the near wellbore region for high-rate flows ("non-Darcy effect"), which has been traditionally modeled by adding a Forchheimer drag term to the Darcy's equation [1, 2]. The Forchheimer drag models the pressure loss of the fluid associated with the converging and diverging nature as well as the tortuosity of the pores in the porous media. If the formation fluid is a compressible gas, a large drop in the pressure over a short distance in the near wellbore region can cause the gas to expand rapidly. This rapid volumetric expansion can induce an additional gas acceleration in the near wellbore region. This volumetric-expansion-induced inertial effect differs significantly from that modeled by the Forchheimer drag. For example, for a steady compressible radial flow, the convective-inertial term in the momentum equation $\rho \, \text{v}_r \frac{\partial \text{v}_r}{\partial r}$ produces a term that is proportional to $\frac{\partial \rho}{\partial r}$, which can be large. This gas-expansion term cannot be obtained from the Forchheimer drag term, and it does not exist for incompressible flows. Furthermore, this gas-expansion effect can cause a highly compressible flow in porous media to become choked at high flow-rates, similar to choked flows in gas dynamics. It has been shown that choking in porous media cannot be predicted from the Darcy-Forchheimer equation, and it is necessary to include gas

3

acceleration in the momentum equation in order to explain such a phenomenon [5 - 8].

Recently, Jin *et al* [9] have studied the possibility of choking for such high flow-rate gas

flows near a wellbore. The physical consequence of a choked or nearly-choked flow is

that the local gas pressure gradient at the point of choking becomes unbounded, while the

pressure drop remains finite. Because of the coupling between the gas flow and the

deformation of the porous rock frame, such a large gas pressure gradient generates an

effective tensile stress on the porous rock frame, which almost always exceeds the tensile

strength of the rock (which is very small), causing a tensile failure (cave-in) of the

wellbore if choking occurs near the wellbore (Jing et el, 2011b; Chen, 2012). Thus,

whether a compressible gas flow in a porous medium is near the choking condition is of

significant importance for gas production in open-hole completed wells.

It is noted that previous investigations of choked flow in gas production by Jin et

al (2012a, b) have utilized the *averaged* momentum equation for the porous media at a

macroscopic scale, i.e. the modified Darcy-Forchheimer equation which maintains

convective acceleration. In reality, however, there is a broad range of pore size

distribution in a porous rock, and not all pores are choked at the same flow-rate (see Fig.

1.2). Even if just one pore in the representative elementary volume (REV) is choked, the

unbounded pressure gradient in this pore will cause the REV-averaged pressure gradient

to become unbounded, while the REV-averaged pressure itself remains well defined and

finite. If we compute the REV-averaged pressure first, and then take the gradient of the

averaged pressure, we will never detect the unbounded pressure gradient present when

one of the pores is choked. In other words, *the gradient of the REV-averaged pressure is*

not the same as the average of the pressure gradient when flow in one of the pores is

4

nearly choked. Thus, as far as the forces exerted by the flowing gas on the porous rock frame is concerned, when just one pore is choked, the flow through the entire REV should be considered choked. This shows the importance of choking at the *pore-scale level* to the macroscopically averaged porous media flow. It is this reason that we propose to study choking condition at a single microscopic pore in this thesis.
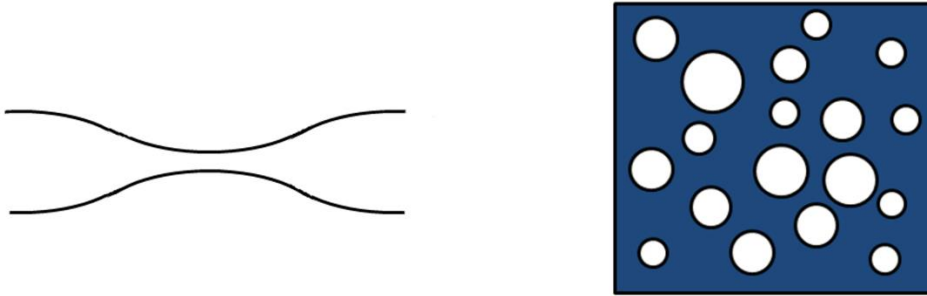
Fig. 1.2 Varicose capillary tube and aross-section of a Representative-Elementary-Volume (REV). A plane perpendicularly intersects with pores with different diameters.

While the real pore geometry is extremely complex and difficult to model, we chose to study a prototype varicose pore, expecting that the results from such a simple pore can provide the needed insights into the more realistic pores. Thus, in this study, we model a pore as a varicose pipe, with multiple bumps

Fig. 1.3 The basic microscopic pore model: A varicose pipe with multiple bumps

Before we present the details of this work on the varicose pore, however, we first review the literature of compressible gas flow in porous media as well as compressible gas flow through a straight pipe.

1.1   Flow in porous media

A porous medium is a material consisting of a solid matrix with an interconnected void. In a natural porous medium the distribution of pores with respect to shape and size is irregular [10]. Flow though porous media is encountered in many branches of engineering and science, e.g., ground water hydrology, oil reservoir engineering, soil science, soil mechanics and chemical engineering.[11] For example, in hydraulic fracturing, which is a process widely used in natural gas well and a topic of current interest in light of the huge success of shale gas production in the US, a fracturing fluid is pumped though a wellbore at a pressure and flow rate at least sufficient to overcome the overburden pressure and to extend a fracture into the rock. The fracturing fluid usually carries a proppant such as sand and bauxite, suspended in the fracturing fluid and transported into a fracture. The proppant then keeps the formation from closing back down upon itself when the pressure is released. The proppant filled fractures provide permeable channels through which the formation fluids can flow to the wellbore and thereafter be withdrawn. [12] The proppant-filled fractures along with the formation fluids are typically modeled as porous media. In soil science, the soil-plant system along with the ground water is another example of porous media.

In typical porous media flow experiments, the quantities of interest are measured over areas that cross many pores, and such space-averaged (macroscopic) quantities change in a regular manner with respect to space and time, and hence are amenable to theoretical treatment. But on the pore scale (the microscopic scale) the flow quantities such as pressure, velocity etc. will be clearly irregular because of the size and shape. [3] At the macroscopic level, the simplest description of the flow of a fluid through a porous

6

medium is the Darcy's law for laminar flow. Henry Darcy (1856) investigated the hydrology of the water supply of Dijon and did experiments on steady-state unidirectional flow in a uniform medium, which was the flow of water through beds of sand. The investigation and experiment revealed a proportion between flow rate and the applied pressure difference. In modern notation this is expressed, in refined form, by

$$\mathbf{v} = -\frac{K}{\mu}\nabla P$$

where $\mathbf{v}$ is the flow-rate per unit medium area or Darcy-velocity (also named seepage velocity), ∇P is the pressure gradient in the flow direction, and μ is the dynamic viscosity of the fluid. K is a coefficient independent of the nature of the fluid but depends on the geometry of the medium. It is called the specific permeability or intrinsic permeability of the medium. For the case of an isotropic medium the permeability is a scalar.[10]

Although Darcy's law was determined experimentally by Darcy, it has been derived from the Navier-Stokes equations via homogenization techniques. Darcy's law along with the equation of conservation of mass is equivalent to the groundwater flow equation, one of the basic relationships of hydrogeology. Darcy's law is also used to describe oil, water, and gas flows through petroleum reservoirs.

While early research has used the Darcy's law to describe the flow of the formation fluids (oil, gas) to the wellbore, or through the propped fractures (Prats, 1961, 1962; Cinco-Ley & Samaniego, 1981), it has been well recognized that inertial effect is important for such flows at high flow-rates. Darcy's equation is linear in the Darcy velocity $\mathbf{v}$. It holds when $\mathbf{v}$ is sufficiently small, which means that the Reynolds number of the flow, based on a typical pore or particle diameter, is of order unity or smaller. As $\mathbf{v}$ increases, the transition to nonlinear drag is quite smooth. The breakdown in linearity is

7

due to the fact that the form drag due to solid obstacles is now comparable with the surface drag due to friction. The inertial effect in such flows has been traditionally accounted for by adding a quadratic drag (Forchheimer drag) to the Darcy's equation, and the resulting Darcy-Forchheimer equation has been the *de facto* standard equation in ground water hydraulics and petroleum engineering throughout the past few decades for treating non-Darcy effects [10]. Indeed, the Darcy-Forchheimer equation has been very successful in many such applications.

The Darcy-Forchheimer equation, however, is not without limitations. For example, in the petroleum engineering literature, fluid compressibility has been taken into account via the continuity equation and by allowing the density in the Darcy-Forchheimer equation to depend on the pressure and temperature via the equation-of-state. This approach, however, only incorporates weakly compressible effect since the fluid compressibility is approximated as a constant instead of pressure-dependent; and convective acceleration caused by gas volume expansion is completely ignored. Normally, a large drop in gas pressure within a short distance to a gas well can cause the gas to expand rapidly. This rapid expansion can induce significant gas acceleration in the near wellbore region for a high pressure gas (see discussions above).[13] This leads to the consideration of the possibility of choked flow in a porous medium. We review first, however, the classical choked gas flow in a clean pipe.

1.2   Fanno flow and choking condition for compressible flow in a pipe

The flow of a compressible fluid in a duct is always accompanied by friction. Friction, heat transfer, and variation in the cross-sectional area of the duct contribute to

changes in the flow properties. Friction is associated with turbulence and viscous shear of molecules of the gas; friction is associated also with the movement of gas molecules near the walls of the duct. Fanno flow is the adiabatic flow of an ideal gas through a constant cross section area duct with friction. It is helpful to describe Fanno flow with a temperature-entropy diagram (T-s). Fig. 3 shows a curve in the T-s plane for a given gas and fixed values of stagnation temperature, cross section area, and inlet temperature, pressure, and entropy. Curves like sketched in Fig. 3 are called Fanno lines.
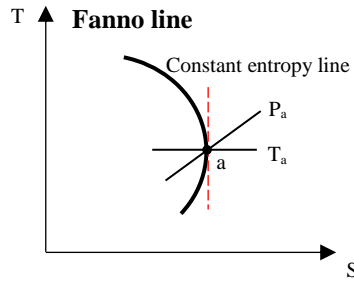
Fig. 1.4 The T-s diagram for Fanno flow

The second law of thermodynamics states that entropy can only remain constant or increase for adiabatic flows. For Fanno flow to be consistent with the second law of thermodynamics, flow can only proceed along the Fanno line towards point "a", the critical state. The critical state may or may not be reached by the flow. If it is, the Fanno flow is choked, and the local pressure gradient is unbounded. In mechanical terms, choking refers to a flow regime when the flow rate reaches a maximum and it no longer increases with further increase in the pressure drop. Analogously, for a gas production well, the radial flow at the macroscopic level can become choked at a high flow rate; and for choked flows, the gas pressure gradient at the wellbore wall can become infinitely large.[7,8] Choked flow in porous media is reviewed below.

9

1.3   Choked flow in porous media: macroscopic description

Perhaps the earliest evidence suggesting that strong compressibility effects can be present in some porous media flows came from the extensive experimental work of Green & Duwez (1951), who showed that nitrogen flow through porous sintered metals can become choked at moderate pressure ratios [14]. Shreeve (1968) studied gas flow through a porous plate, and he found that such a flow can become choked and shock wave can form at a high flow-rate [15]. Emanuel & Jones (1968) developed a theory analogous to Fanno flow to explain the findings of Shreeve (1968). This work demonstrated the necessity of incorporating gas convective acceleration in the momentum equation in order to explain the choking phenomenon [16]. Beavers & Sparrow (1971), Meyer & Smith (1985) studied analytically and experimentally steady compressible flows through a porous medium, focusing on the choking condition. Beavers & Sparrow (1971) found that the Mach number based on the gas intrinsic velocity just inside the entrance to a porous medium can be significantly higher than the Mach number ahead of the entrance due to the contraction in the flow area. This makes the flow more susceptible to choking. Meyer & Smith (1985) measured the threshold value for the pressure ratio for choked flow in a porous medium and constructed a constant cross-sectional area conduit model to predict the choking condition [13, 17]. Kodres (1994) proposed a flow-rate and pressure ratio relation based on a constant cross-sectional area conduit model for compressible heated gas flow through porous media which incorporated the choking phenomenon [18]. Nield (1994) discussed in detail suitable models for high speed compressible flows in a porous medium. He argued that the Darcy-Forchheimer equation is not adequate for such flows since inertia associated

with gas convective acceleration can become important for compressible flows at a high speed. He showed that without the convective acceleration in the momentum equation, choking cannot be predicted [19 - 21]. The work of de Ville (1996) further demonstrated quantitatively that, although both are of inertial origin, the convective acceleration and the Forchheimer drag play distinctly different roles in one-dimensional isentropic compressible flows in porous media: while the Forchheimer drag always retards the flow, the convective acceleration can aid the flow in certain situations. Choking was also shown to occur in two-dimensional flows when gas acceleration becomes large. Choking will not occur in the absence of convective acceleration [22]. Levy *et al* (1995) took a rigorous approach and established governing equations for compressible flow through *deformable* porous media. The momentum equation of Levy *et al* (1995) maintains the full convective inertial term and has the Forchheimer term arising naturally from a quadratic term at the fluid-solid interface. While the approach of Levy *et al* (1995) is more rigorous, the fact that the Forchheimer term arises from the fluid-solid interface is consistent with the view that it is a drag force caused by inertial effect, which was modeled in an *ad hoc* fashion by many authors (Nield, 1994) [21, 23]. Thus, there is no fundamental difference in the resulting model equations proposed by various authors. We also noticed that Ciarletta & Straughan (2006) and Straughan (2008) have derived the Jordan-Darcy equation (Jordan, 2005) from the mixture theory which maintains the full convective term. The addition of the Forchheimer term is therefore a natural extension of this kind of theory [24 – 25].

More recently, Jin et al (2010, 2012) have investigated high pressure compressible gas flow towards a wellbore in a porous medium (Jin *et al* 2010, 2012). They found that

for high pressure, high permeability gas reservoirs, gas acceleration near the wellbore can become so large that it influences the overall flow significantly. They found a condition under which gas acceleration has to be retained in the momentum equation, and demonstrated significant changes in the pressure-flow-rate relation for such flows. When gas compressibility becomes important, gas flow-rate is limited by the choking phenomenon. In addition, the pressure gradient at the wellbore wall can become very large, and unbounded for choked flows. Large gas pressure gradient at the wellbore wall has significant implications for the stability of the wellbore and the onset of sand production due to possible tensile failure of the formation rocks [26 – 29]. Since the pore pressure and the radial stress are both equal to the wellbore pressure at the wellbore wall, the Terzaghi effective radial stress is zero at the wellbore wall. Thus, if the gradient of the pore pressure is larger than the gradient of the radial stress, the pore pressure will be larger than the radial stress near the wellbore, causing the Terzaghi effective radial stress to become negative, or tensile, in the vicinity of the wellbore wall. This region of effective tensile stress can cause a tensile failure of the formation rocks because of the low tensile strength of the formation rocks. This kind of tensile failure mechanism has been discussed in detail in the literature [30 -33]. What sets apart the high pressure, high speed gas flow from other applications is that the existence of such a tensile region near the wellbore is *guaranteed* if the flow is near the choking flow condition, due to the unbounded pore pressure gradient at the wellbore wall. It is also noted that in soil mechanics, the appearance of a tensile stress caused by seepage or hydrodynamic force can lead to reveling, piping, or liquefaction of the soil. [34]

1.4   Scope of the Thesis

Choked flow is undesirable during petroleum production as it can lead to mechanical damage/failure of the wellbore. As discussed above, as far as the forces exerted by the flowing gas on the porous rock frame is concerned, when just one pore is choked, the flow at the macroscopic level should be considered choked. All existing works, however, have employed the macroscopic equations which are clearly incapable of describing the situation of choking at the pore-scale level.

The main focus of the present thesis is to identify the choking condition for a compressible gas in a porous medium by studying pore-scale compressible flow. The basic model will be a long and narrow duct with bumps on the wall. The number of bumps, the amplitude of bumps, and the length of the duct are the factors to be considered. Simulations will be carried out to find how these factors affect the choking condition.

1.5   Organization of the Thesis

Chapter 2 presents the mathematical formulation and methodology used; and Chapter3 gives the main results of this thesis. The thesis ends with a summary in Chapter 4.

CHAPTER 2   MECHMATICAL METHOD

2.1   One-dimensional theory

2.1.1   Basic model and governing equations for quasi-one-dimensional flow

A bundle of capillary tubes is frequently used as a simple pore-scale model for porous media (Jacob, 1970). For example, the flow through a propped- fracture is shown in Fig 2.1. Gas flows through the fine gaps between sand particles.
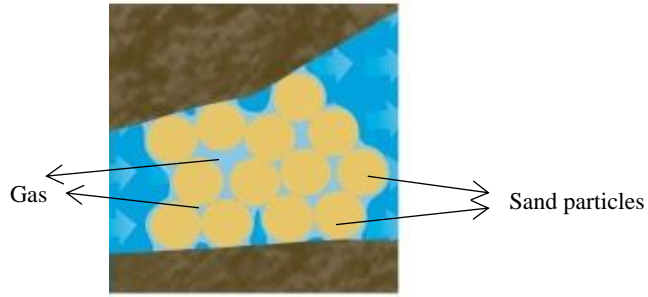

Fig 2.1 A physical model for the flow in a sand propped fracture.

The proppant-filled fracture can be considered as a porous medium composed of numerous curved capillary tubes. Consider flow through one single microscopic tube. We build a symmetric varicose tube model with the first half of the tube being straight and the other half with varicose curve shown below in Fig. 2.2.
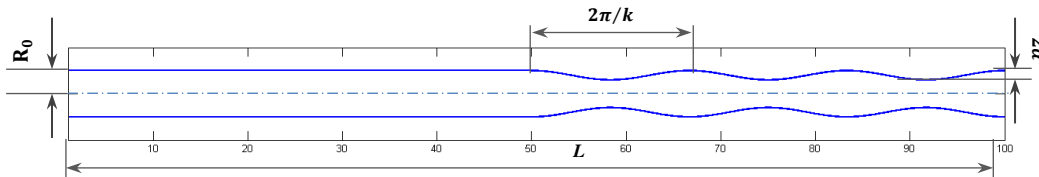

Fig 2.2 Geometric model of the flow in pipe

The equation describing the variation of the radius is:

$$R(x) = R_0 - \alpha \cdot \frac{1 + \tanh\left[b\left(x - \frac{L}{2}\right)\right]}{2} \cdot \left[1 - \cos k\left(x - \frac{L}{2}\right)\right] \qquad (2.1)$$

where x represents the position along the axis. R_0 is the original radius of the duct. L is the length of the duct. α is the amplitude of the bump, k controls the wave number of the curved portion of the tube. b is set to be a constant, and the term $\frac{1+\tanh\left[b\left(x-\frac{L}{2}\right)\right]}{2}$ is used to connect the straight part and varicose part of the tube smoothly. In our computations, we set b = 30.

To simplify the calculation, the formation fluid in the microscopic duct is modeled as an ideal gas. The generalized one-dimensional compressible flow can be described mathematically using the following conservation equations. These equations are applicable to study the combined effect of area change and friction in a constant area duct as well as in a various area duct.

The continuity equation is:

$$\frac{d\rho}{\rho} + \frac{dA}{A} + \frac{dV}{V} = 0 \tag{2.2}$$

The momentum equation is:

$$\frac{dp}{p} + \frac{\gamma M^2}{2}\frac{4f\,dx}{D_H} + \rho V dV = 0 \tag{2.3}$$

where $\gamma = \dfrac{c_p}{c_v}$ is the heat capacity ratio, 4f is the friction factor, D_H is the hydraulic diameter. We also introduce a local Mach number

$$M = \frac{V}{a} \tag{2.4}$$

where V is the velocity of the gas, $a = \sqrt{\gamma RT}$ is the speed of sound.

Using the definition of Mach number and stagnation temperature, equations (2.2) and (2.3) can be expressed as an ordinary differential equation of 1st order with regard to Mach number and variable area along x axis.

$$\frac{dM}{dx} = \frac{M(1+\frac{\gamma-1}{2}M^2)}{1-M^2}\left[\gamma M^2\frac{4f}{D} + \frac{(1+\gamma M^2)}{2T_0}\frac{dT_0}{dx} - \frac{1}{A}\frac{dA}{dx}\right] \qquad (2.5)$$

$\frac{dT_0}{dx}$ in equation (2.5) can be determined from energy equation which can be expressed as

$$q(\pi D)dx = \dot{m}c_p dT_0 \qquad (2.6)$$

where q is the heat flux at the pipe wall. Since we are considering adiabatic flow, the heat flux at the pipe wall is zero. Thus

$$\frac{dT_0}{dx} = 0 \qquad (2.7)$$

Given the inlet condition $M(x = 0) = M_1$, the 1st order differential equation (2.5) in M can be solved to find the Mach number at any location x. When M reaches 1.0, the flow is choked.

Changes in temperature and pressure can be determined from the following equations:

$$\frac{dT}{T} = -(\gamma - 1)\frac{M\ dM}{1 + \frac{\gamma-1}{2}M^2} \qquad (2.8)$$

$$\frac{dp}{p} = \frac{1}{2}\frac{dT}{T} - \frac{dA}{A} + \frac{dM}{M} \qquad (2.9)$$

With the 1D analysis above, we can obtain the profile of Mach number, the temperature and the pressure ratio along the duct under the effect of constant friction and a variety of cross-sectional areas [35].

2.1.2 Non-dimensionalization

For adiabatic flow of an ideal gas, we introduce the following length and pressure scales:

$$R_0 = x_f, \qquad p_{in} = p_f \tag{2.10}$$

We define the following dimensionless quantities,

$$\bar{x} = \frac{x}{x_f}, \ \ \bar{L} = \frac{L}{x_f}, \ \ \bar{a} = \frac{a}{x_f}, \ \ \bar{k} = k \cdot x_f, \ \ \bar{p} = \frac{p}{p_f} \tag{2.11}$$

To simplify the calculations, the two segments of the pipe are analyzed separately. The first part is a straight pipe, the other part of the pipe has cosine curved wall:

When $x < \frac{L}{2}$,

$$\frac{dM}{M} = \frac{1}{2} \frac{1 + \frac{\gamma - 1}{2} M^2}{1 - M^2} \gamma M^2 \frac{4f d\bar{x}}{2\bar{R}} \tag{2.12}$$

where $\bar{R} = \frac{R}{R_0} = 1$.

When $x \geq \frac{L}{2}$,

$$\frac{dM}{M} = -\frac{1 + \frac{\gamma - 1}{2} M^2}{1 - M^2} \cdot \frac{-2\bar{a}\,\bar{k}\sin\bar{k}\left(\bar{x} - \frac{\bar{L}}{2}\right)}{\bar{R}} + \frac{1}{2} \frac{1 + \frac{\gamma - 1}{2} M^2}{1 - M^2} \gamma M^2 \frac{4f d\bar{x}}{2\bar{R}} \tag{2.13}$$

where $\bar{R} = 1 - \bar{a}\left[1 - \cos\bar{k}\left(\bar{x} - \frac{\bar{L}}{2}\right)\right]$.

From the equations above, it can be easily found that the variation of Mach number along the x axis is a function of $\bar{L}, \bar{k}, \bar{a}$, as well as the pressure ratio, which will affect the inlet Mach number. In the simulations, we will study how these parameters affect the choking condition.

2.2   CFD simulation

In order to fully understand the complicated flow through the curved duct near choking condition and the factors that cause the flow to become choked, the approximate quasi-one-dimensional theory may not be accurate enough and a high resolution solution for velocity, pressure and temperature distributions may be required. To this end, we will use more powerful computational fluid dynamics (CFD) tools to study the choking condition.

2.2.1   Geometry and mesh generation

The axisymmetric geometry of the pipe is shown in Fig. 2.2. In this work, we will change the parameters $\bar{a}, \bar{L}, \bar{k}$ and study how these parameters affect the choking condition. Since the pipe is modeled as axisymmetric, only the upper half of the pipe is considered in the simulation.

In CFD, there are essentially three different meshes: structured mesh, unstructured mesh and half-structured mesh. Using structured mesh, we can control the density of the mesh in any direction; however, such a meshing method may not be able to adapt to complicated shape. Unstructured mesh adapts well to complicated shape. The operation is easy, but meshing quality is not as good as structured mesh. Half-structured mesh is a combination of structured and unstructured mesh. It uses structured mesh in the area with regular shape, and unstructured mesh in irregular areas. Normally, numerical computation has the following three requirements for mesh generation: body-fitted, smooth, reasonable density and good orthogonality.

In the current geometric model, the structure is not complicated, and structured mesh is the best choice. High quality of the mesh near the axis is important to obtain

accurate velocity and pressure profile on choking condition, especially around the choking area. The mesh is mainly uniform, and grids near the axis and wall are finer, as shown in Fig. 2.3.
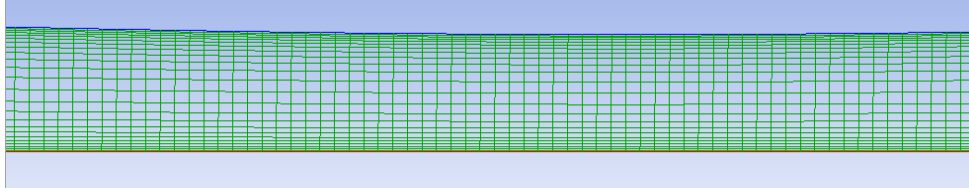

Fig. 2.3 Part of the Mesh Scheme

2.2.2　Governing equation, basic numerical method in FLUENT

The Reynolds number of our model is around 10^5 to 10^6 based on a rough estimate. Since we are investigating the condition approaching choked flow, the flow is still subsonic. The chocking area where the Mach number approaches 1.0 is referred to as the transonic flow regime, where compressibility effects become important.

Compressible flow is governed by the continuity, Navier-Stokes, energy and state equations where all the fluid properties are variable. For turbulent compressible flow, these governing equations are essentially time-averaged using RANS method and the resulting solution is for the mean quantities. The equations can be solved using an appropriate turbulence model. For steady two-dimensional mean flow, the governing equations of the turbulent model can be expressed in terms of tensor notation as follows:

(1) The continuity equation is given by:

$$\frac{\partial}{\partial x_j}(\rho \bar{u}_j) = 0 \qquad (2.14)$$

(2) The Navier-Stokes equations are given by:

$$\frac{\partial}{\partial x_j}\left(\rho \overline{u_j} \overline{u_\iota}\right) = \frac{\partial}{\partial x_j}\left(t_{ij} + \tau_{ij}\right) - \frac{\partial p}{\partial x_i} \tag{2.15}$$

where t_{ij} and τ_{ij} are the laminar and turbulent stresses, respectively, with the following definitions :

$$t_{ij} = \mu\left[\left(\frac{\partial \overline{u_\iota}}{\partial x_j} + \frac{\partial \overline{u_j}}{\partial x_i}\right) - \frac{2}{3}\delta_{ij}\frac{\partial \overline{u_k}}{\partial x_k}\right] \tag{2.16}$$

where μ is the fluid viscosity, δ_{ij} is the Kronecker delta: $\delta_{ij} = 0$ when $i \neq j$ and $\delta_{ij} = 1$ when $i = j$; and

$$\tau_{ij} = \mu_t\left[\left(\frac{\partial \overline{u_\iota}}{\partial x_j} + \frac{\partial \overline{u_j}}{\partial x_i}\right) - \frac{2}{3}\delta_{ij}\frac{\partial \overline{u_k}}{\partial x_k}\right] - \frac{2}{3}\delta_{ij}\rho k \tag{2.17}$$

where μ_t is the turbulent viscosity and k is the kinetic energy of turbulence. μ_t is computed by combining k and ε as follows:

$$\mu_t = \rho C_\mu \frac{k^2}{\varepsilon} \tag{2.18}$$

C_μ is the model constant, and ε is the dissipation rate of k. Standard *k-epsilon* model is suitable for our model and it is one of the most commonly used turbulence models in commercial CFD.

(3)   Two Transport equations

The standard $k - \varepsilon$ model is a model based on model transport equations for the turbulence kinetic energy (k) and its dissipation rate (ε).

In the derivation of the $k - \varepsilon$ model, the assumption is that the flow is fully turbulent, and the effects of molecular viscosity are negligible. The turbulence kinetic

energy, k, and its rate of dissipation, ε, are obtained from the following transport equations:

$$\frac{\partial}{\partial x_i}(\rho k \bar{u}_\iota) = \frac{\partial}{\partial x_j}\left[\left(\mu + \frac{\mu_t}{\sigma_k}\right)\frac{\partial k}{\partial x_j}\right] + G_k + G_b - \rho\varepsilon - Y_M \qquad (2.15)$$

$$\frac{\partial}{\partial x_i}(\rho\varepsilon\bar{u}_\iota) = \frac{\partial}{\partial x_j}\left[\left(\mu + \frac{\mu_t}{\sigma_\varepsilon}\right)\frac{\partial\varepsilon}{\partial x_j}\right] + C_{1\varepsilon}\frac{\varepsilon}{k}(G_k + C_{3\varepsilon}G_b) - C_{2\varepsilon}\rho\frac{\varepsilon^2}{k} \qquad (2.16)$$

In these equations, G_k represents the generation of turbulence kinetic energy due to the mean velocity gradients, G_b is the generation of turbulence kinetic energy due to buoyancy, Y_M represents the contribution of the fluctuating dilatation in compressible turbulence to the overall dissipation rate. $C_{1\varepsilon}$, $C_{2\varepsilon}$, $C_{3\varepsilon}$, σ_k and σ_ε are constants.

The model constants $C_{1\varepsilon}$, $C_{2\varepsilon}$, C_μ, σ_k and σ_ε have the following default values:

$$C_{1\varepsilon} = 1.44, \qquad C_{2\varepsilon} = 1.92, \qquad C_\mu = 0.09, \qquad \sigma_k = 1.0, \qquad \sigma_\varepsilon = 1.3$$

These default values have been determined from experiments for fundamental turbulent flows including frequently encountered shear flows like boundary layers, mixing layers and jets as well as for decaying isotropic grid turbulence. They have been found to work fairly well for a wide range of wall-bounded and free shear flows.

(4) Energy equation is given by:

$$\frac{\partial}{\partial x_j}(\rho\bar{u}_j e_T) = \frac{\partial}{\partial x_j}\left[\left(\frac{k_T}{c_v} + \frac{\mu_t}{Pr_t}\right)\frac{\partial e_T}{\partial x_j}\right] + \frac{\partial}{\partial x_j}\left[\bar{u}_\iota(t_{ij} + \tau_{ij})\right] - \frac{\partial}{\partial x_j}(\bar{u}_j p)$$

$$+ \frac{\partial}{\partial x_j}\left[\left(\mu + \frac{\mu_t}{\sigma_k}\right)\frac{\partial k}{\partial x_j}\right] - \frac{\partial}{\partial x_j}\left[\left(\frac{k_T}{c_v} + \frac{\mu_t}{Pr_t}\right)\frac{\partial k}{\partial x_j}(K + k)\right] \quad (2.17)$$

where k_T is the thermal conductivity, c_v is the specific heat at constant volume, Pr_t is the turbulent Prandtl number taken as 0.91, and e_T is the total energy which is defined as

21

$e_T = e + K + k$. Where e is the internal energy ($c_v T$) and K is the kinetic energy of the mean flow, $K = 0.5(\bar{u}^2 + \bar{v}^2)$ [36 -38].

2.2.3 FLUENT simulation

(1)　Using the solver.

In ANSYS FLUENT, two solver technologies are available: pressure-based and density-based. Both solvers can be used for a broad range of flows, but in some cases one formulation may perform better. The pressure-based solver traditionally has been used for incompressible and mildly compressible flows. The density-based approach, on the other hand, was originally designed for high-speed compressible flows. Both approaches are now applicable to a broad range of flows (from incompressible to highly compressible), but the origins of the density-based formulation may give it an accuracy (that is shock resolution) advantage over the pressure-based solver for high-speed compressible flows. Thus we choose the density-based solver for this research. The simulation is steady state and the model is axisymmetric.

(2)　 Choosing the viscous model.

As discussed in 2.2.2, the standard *k-epsilon* is chosen as our viscous model. Standard k-epsilon model becomes the workhorse of practical engineering flow calculations because of its robustness, economy, and reasonable accuracy for a wide range of turbulent flows. The turbulent kinetic energy, k is calculated by

$$k = \frac{3}{2}(u_{avg}I)^2 \tag{2.18}$$

where u_{avg} is the mean flow velocity, I is the turbulent intensity defined as the ratio of the root-mean-square of the velocity fluctuations, u', to the mean velocity, u_{avg}. The turbulence intensity at the core of a fully-developed duct flow can be estimated from the following formula derived from an empirical correlation for pipe flows:

$$I = \frac{u'}{u_{avg}} = 0.16(ReD_H)^{-1/8} \qquad (2.19)$$

At a Reynolds number of about 10^5, the turbulence intensity is 4%.

(3) Boundary conditions.

First, the operating pressure is set to be zero, because operating pressure is less significant for higher-Mach-number compressible flows. The pressure changes in such flows are much larger than those in low-Mach-number compressible flows. It is conventional to use absolute pressure in such calculation. Also, for the gas flow in the pipe, gravity can be ignored compared to the high pressure.

The inlet temperature is 300K; the thermal condition is adiabatic. For all models, the inlet static pressure is set to be 10MPa, the input total pressure will be calculated by

$$P_0 = P\left(1 + \frac{\gamma - 1}{2}M_1^2\right)^{\gamma/(\gamma-1)} \qquad (2.20)$$

M_1, as well as the outlet pressure of choking condition can be estimated from 1D analysis.

(4) Setting fluid material.

In the current work, the fluid is modeled as an ideal gas, and gravity is not considered.

23

(5)   Solution methods

The difficulties associated with solving compressible flows are a result of the high degree of coupling between the flow velocity, density, pressure and energy. Pressure option is set as standard, and the pressure-velocity coupling option is set to the SIMPLE algorithms. Reasonable limits for the temperature and pressure are set to avoid solution divergence. The momentum, turbulent kinetic energy, turbulent dissipation rate and energy equation are set as first order upwind.

(6)   Standard of convergence

The convergence criteria about continuity equation and velocity on x, y directions are both 10^{-4}, the convergence criteria of the energy equation is 10^{-5}.

After finishing all the settings above and executing the initialization, the numerical simulation begins. After about 20,000 iterations, the residuals of different variables meet the convergence criteria.

2.2.4   Convergence and grid independence study

There are differences between numerical simulation solution and the exact solution, which are mainly caused by discretization error. The magnitude of the discretization error is related to the truncation error. Under the same time step, the discretization error becomes smaller along with finer mesh. In general, the mesh used for numerical computation needs to satisfy the requirement that the residual stays the same upon further refinement of the mesh.

Grid independence analysis is to check the influence of the size of the grid on the numerical simulation result. One of the representative values, the maximum Mach number in the pipe, is chosen to check whether the grid is fine enough for the simulation. The trial

24

model is the simplest model with one bump and $\bar{L} = \frac{L}{x_f} = 200$. First, we keep the grid

uniform and change the number of nodes in both x and y directions. The grid is refined 7

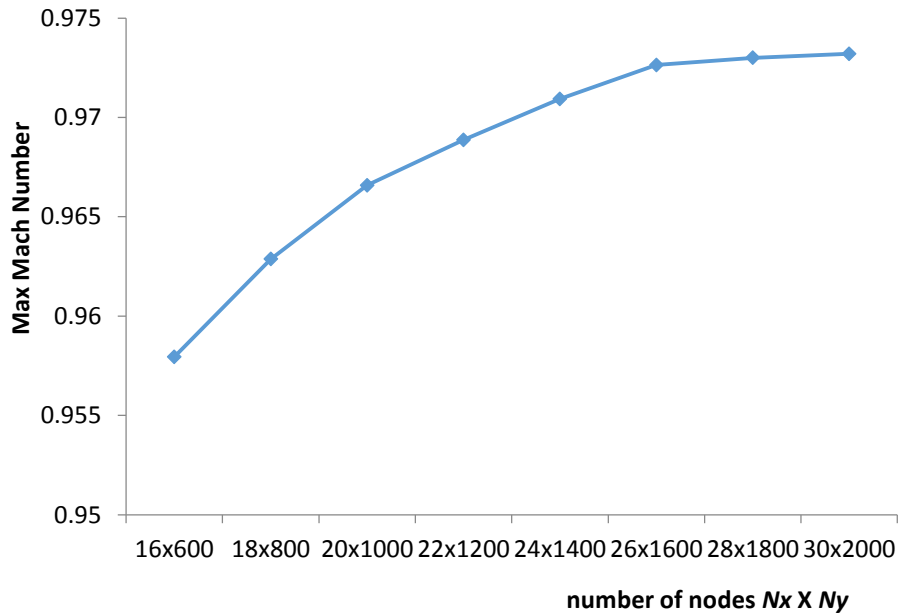times, and the results are shown in Fig.2.2 below.

Fig. 2.4 Grid independent check

As shown in Figure 2.4, when the number of nodes are 26x1600, the maximum Mach

number stays nearly unchanged with further mesh refinement, which indicates the uniform

grid is fine enough for an accurate simulation.

CHAPTER 3 RESULTS AND DISCUSSIONS

3.1   One-dimensional Analysis

First, a basic model with only one bump is selected to study under what condition the flow will become choked (Fig. 3.1). The friction factor is set to be 0.002, the radius is $R_0 = x_f = 0.5cm$, the inlet static pressure is $p_i = 10MPa$, $\bar{L} = 200$, $\bar{\alpha} = 0.1$, $\bar{k} = \frac{\pi}{50}$. Based on the equations (2.5) and (2.9), with a given initial Mach number, the Mach number as well as the pressure along the x axis will be calculated.
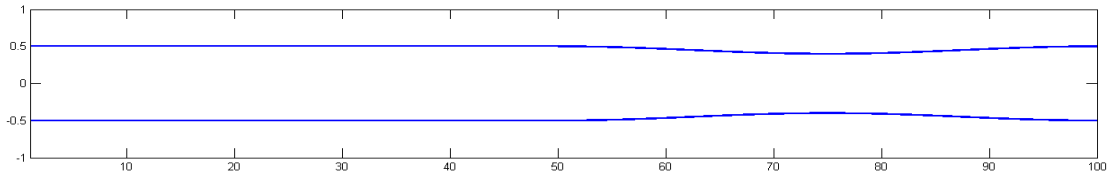
Fig. 3.1 Geometry of the basic pipe

At any cross-section, the Mach number is a maximum at the centerline. The centerline Mach number changes along the tube for any given outlet-to-inlet pressure ratio. As shown in Fig. 3.2, as the prescribed outlet-to-inlet pressure ratio decreases, the maximum Mach number along the x-axis increases. When this pressure ratio drops to 0.8069, the Mach number reaches unity, indicating the flow is being choked.
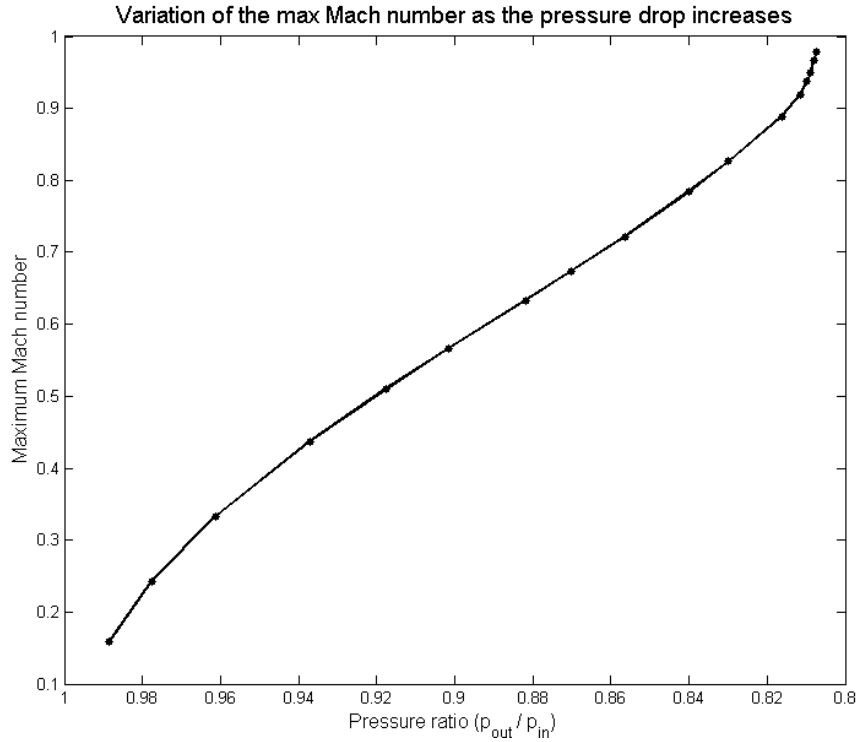
Fig. 3.2 Variation of max Mach number as the initial Mach number increases

This choked flow condition is established at the point of minimum flow area. In our case, the maximum Mach number approaches 1.0 when the entrance Mach number is about 0.36272, which corresponds to a pressure ratio $p_{out}/p_{in} = 0.8069$. Mach number increases as the duct converges, and in the subsequent area expansion the flow returns to subsonic flow conditions, decelerating with a pressure rise. The variation of the Mach number and pressure ratio along the x-axis at this choking condition is shown in Fig. 3.3 and Fig.3.4, respectively
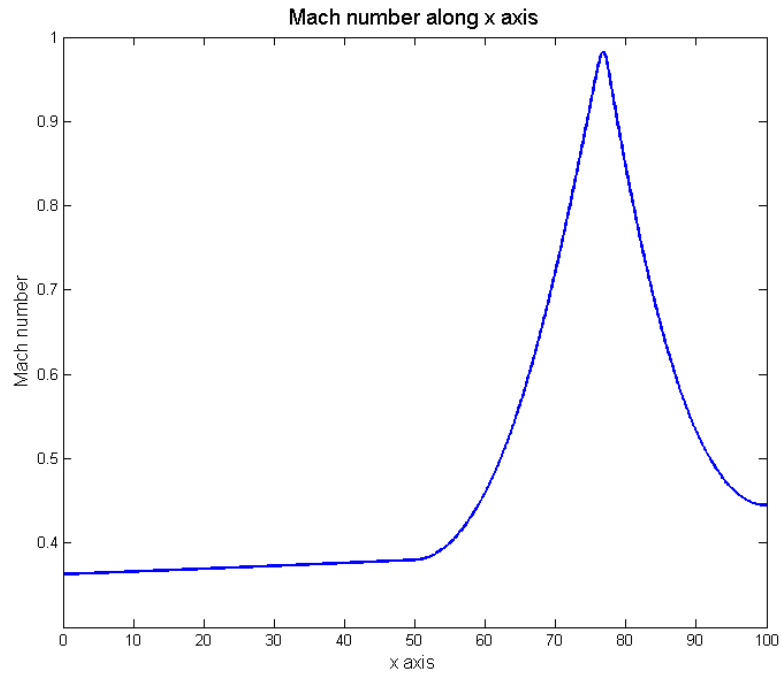
Fig. 3.3 Mach number along x-axis at choking condition
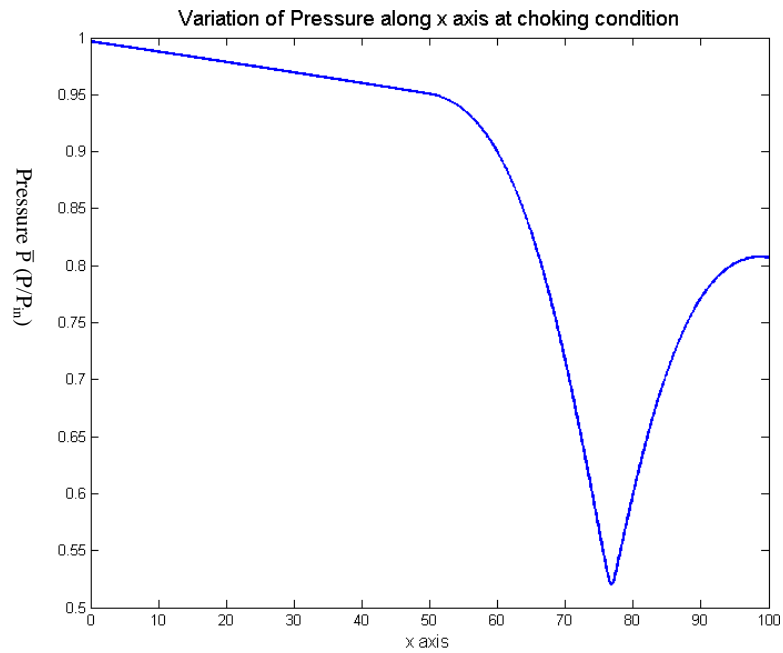
Fig. 3.4 Pressure ratio along x axis at choking condition

3.2 ANSYS FLUENT Two-dimensional Analysis

For the same model as in 3.1, the inlet and outlet pressures used as the boundary conditions for the 2D simulation can be estimated from the 1D analysis. The results converged after about 20,000 iterations. The Mach number contour of the top half of the duct is shown below.
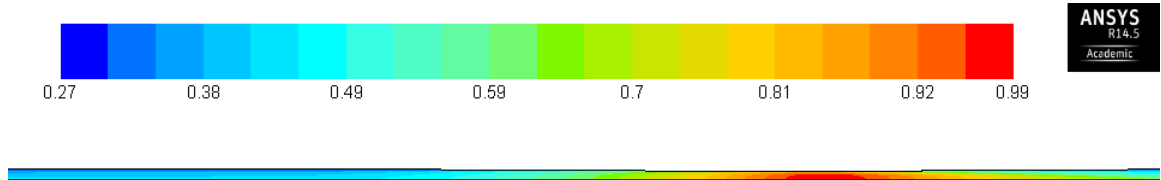

Fig. 3.5 Contour of Mach number along the tube. The Mach number color scale is posted above the contour plot. Choking occurs at the minimum tube area, located at x = 76.5.

It is known that the maximum velocity occurs on the axis of the duct, the variation of Mach number and pressure along the axis is shown below.

Fig. 3.6 Variation of Mach number along the axis
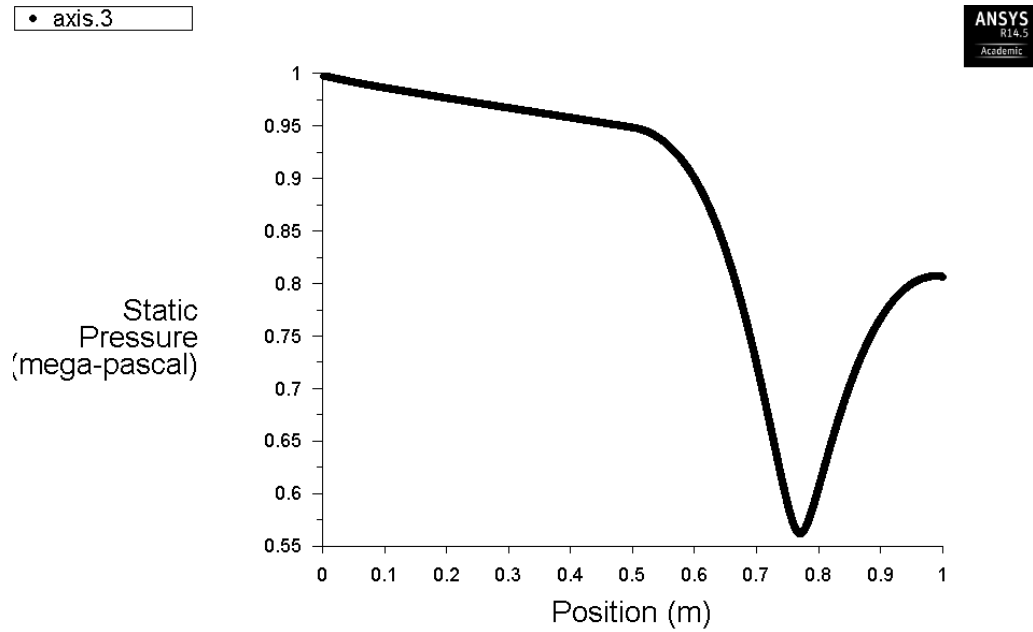
Static
Pressure
(mega-pascal)
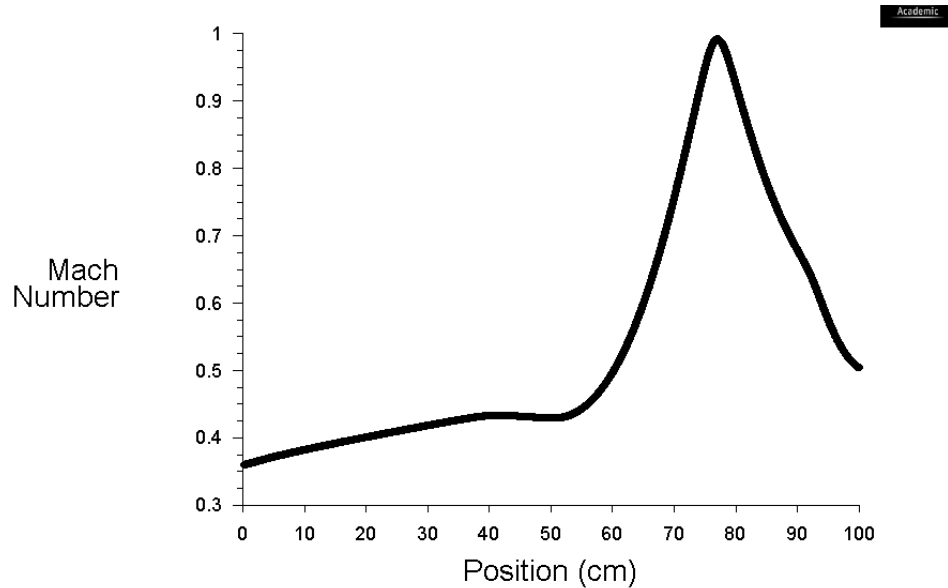
Fig. 3.7 Variation of Pressure along the axis

From the figures above, it's obvious that the shapes of the Mach number and pressure ratio curves are similar to those obtained from the 1D analysis. Comparison between 1D and 2D simulations are shown in Fig. 3.8, and Fig. 3.9 for the Mach number and the pressure, respectively. It is observed that except the peak Mach number, there are considerable differences in the computed Mach numbers, in particular, the exit Mach numbers. The 1D analysis always under-predicts the Mach number. On the other hand, the pressure predictions agree with each other quite well, except the pressure at the point of choking.
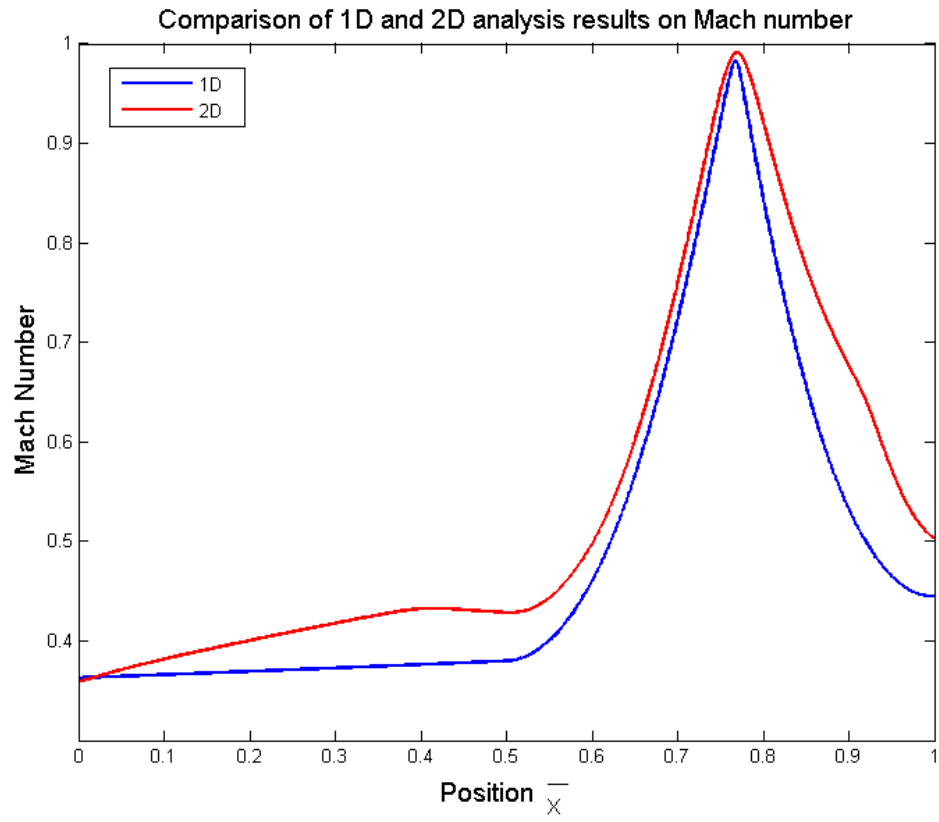
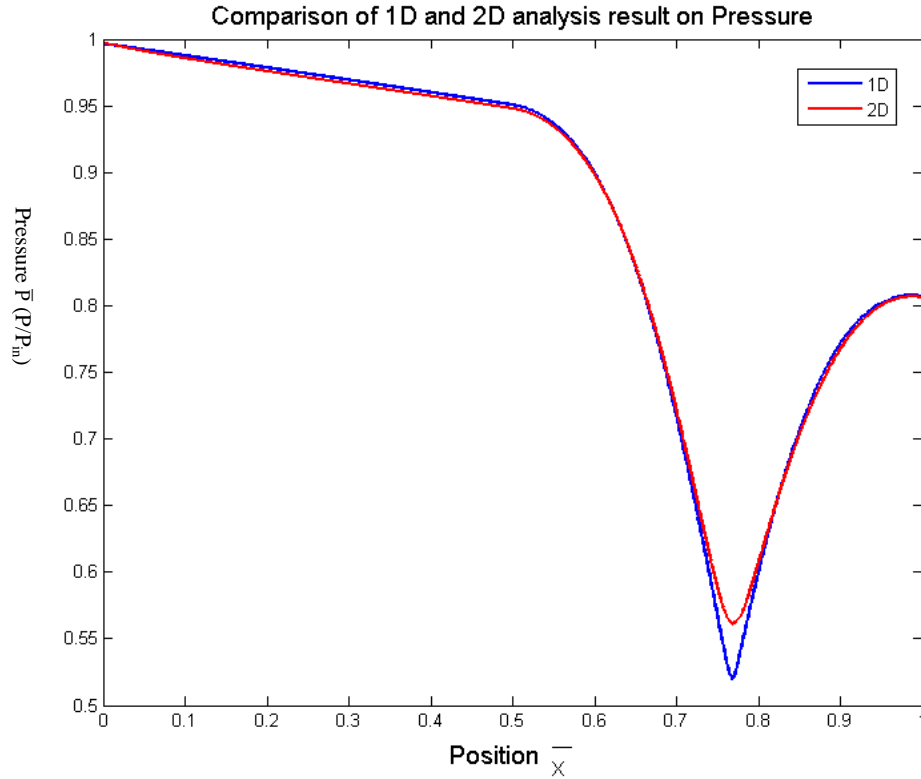Fig. 3.8 1D and FLUENT 2D results comparison for Mach number

Fig. 3.9 1D and FLUENT 2D results comparison for pressure ratio.

3.3   Results and Discussions

Many simulations have been performed to explore how the length, the size of the bump and the number of bumps affect the choking condition. When the radius of the duct is fixed to 0.5cm, these variations will be reflected in the changes in the dimensionless parameters $\bar{L}, \bar{a}, \bar{k}$. In all calculations, the inlet static pressure is fixed at 10 MPa, and we search for the choking conditions.

First, the size of bump and number of bumps are fixed, $\bar{\alpha} = 0.1, \bar{k} = \frac{\pi}{50}$. For 5 models with different lengths, the choking condition all occurs in the narrowest place along the duct. While they all have the same entrance pressure, the corresponding entrance and exit Mach numbers, as well as the exit pressure, are all different. Fig. 3.10

32

shows the centerline Mach number variation along the tube for each of these five different tubes when the flow is choked.
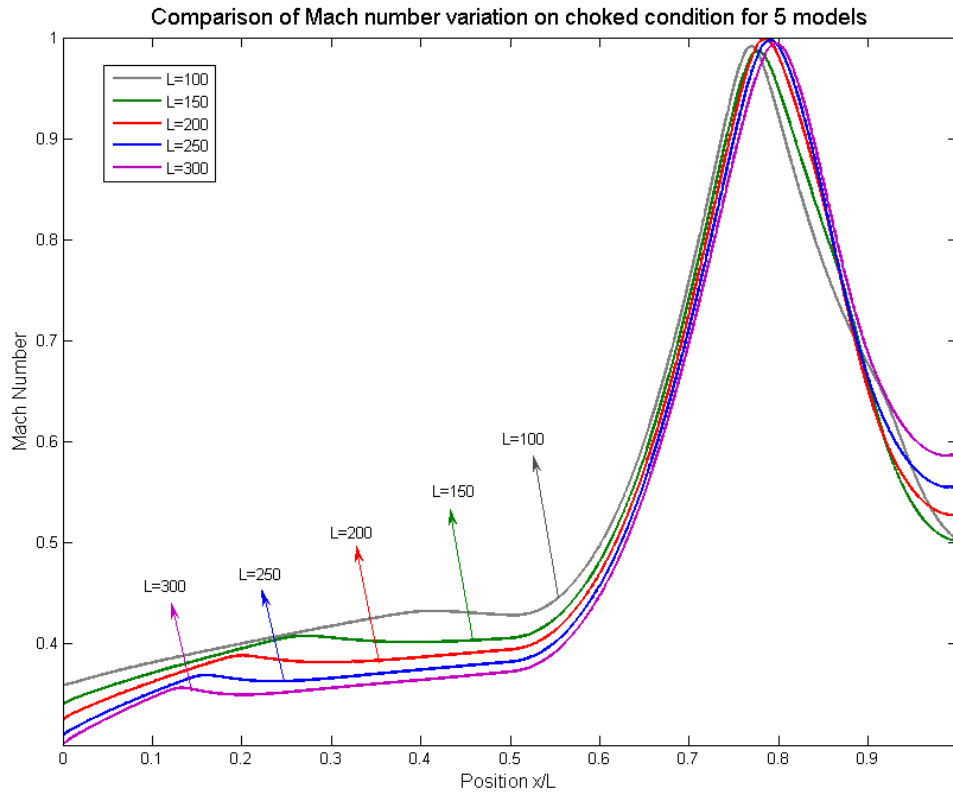

Fig. 3.10 Comparison of the Mach number variation curves at the choking condition for 5 pipes

The Mach number comparison curves show that for longer tubes, the inlet Mach number needed for the flow to reach choking condition is smaller. At the same time, the outlet exit Mach number is larger for the longer duct. This is due to the fact that a longer pipe allows the air to gain more energy from friction.
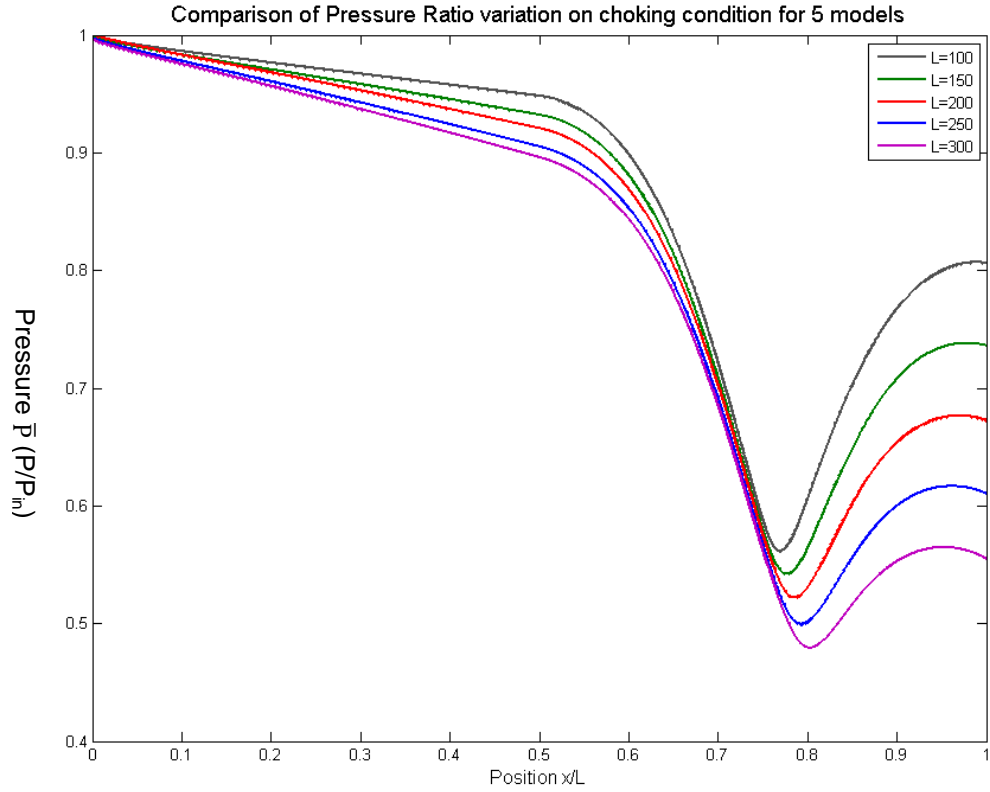
Fig. 3.11 Comparison of pressure ratio variation curve at the choking condition

for 5 different pipes

Fig. 3.11 shows the accompanying pressure variation curves along the tube. It is observed that when the inlet pressure is fixed, the longer the duct, the lower the exit pressure. In other words, a higher inlet-to-outlet pressure ratio is required for the flow to become choked at the minimum area cross-section. Fig. 3.12 shows the variation of the critical pressure ratio P_{in}/P_{out} for choking as a function of the pipe length when the amplitude of bump is $\bar{\alpha} = 0.1$.
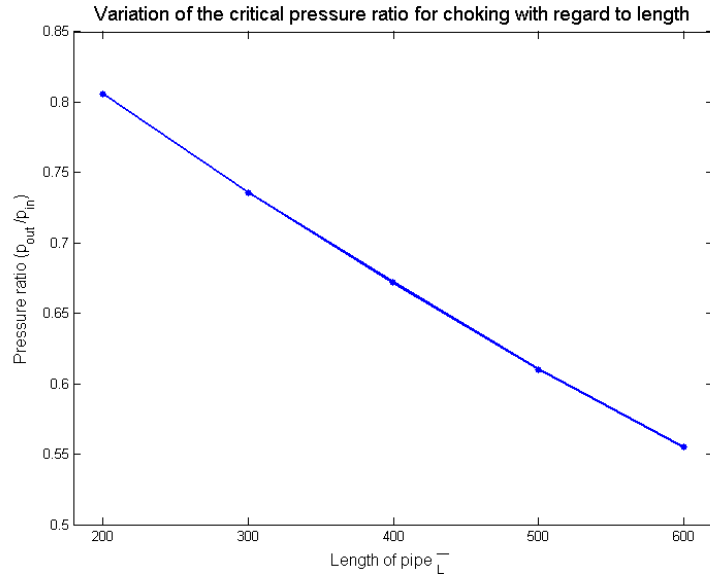
Fig. 3.12 Variation of the critical pressure ratio for choking with regard to length

The amplitude of the bump is also an important factor that needs to be considered. The parameter α controls the size of bump. For each length of the model, we compute for $\bar{\alpha} = 0.1, \bar{\alpha} = 0.2, \bar{\alpha} = 0.3$.
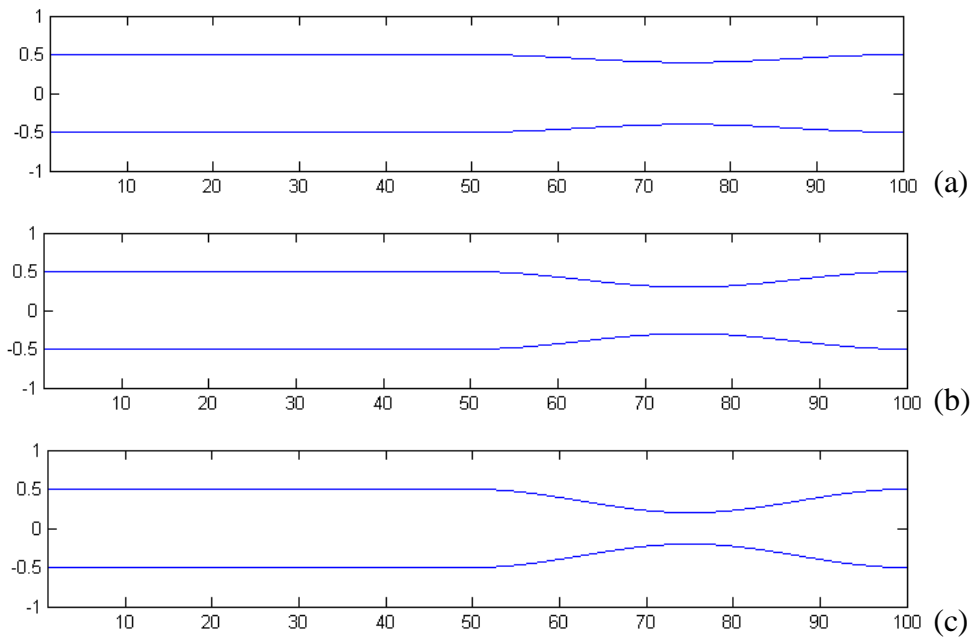

Fig 3.13 (a) Geometry of pipe with $\bar{\alpha} = 0.1$ (b) $\bar{\alpha} = 0.2$ (c) $\bar{\alpha} = 0.3$

Several simulations have been carried out to find the pressure ratio and variation of Mach number along the duct at the choking condition, which are shown in Fig. 3.14 and Fig. 3.15.
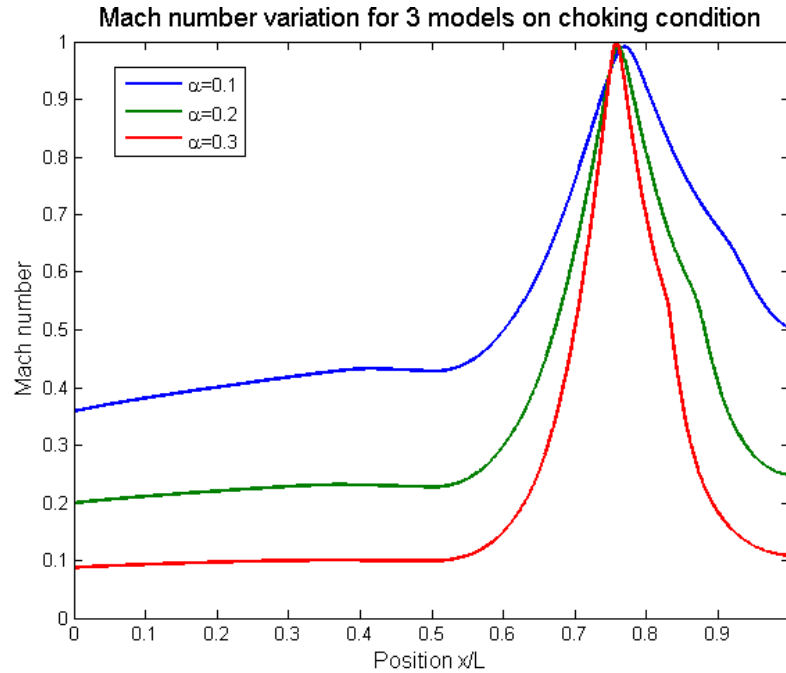

Fig 3.14 Mach number variation for 3 models on choking condition

From the Fig. 3.14 above, it can be seen that choking condition still occurs at the same cross-section for models with different amplitudes. For bumps with a larger amplitude, Mach number increases faster since the cross-sectional area decreases faster. Thus, choking condition could occur with a lower inlet flow velocity. Fig. 3.15 for the pressure variation for the 3 models on choking condition shows that for larger amplitude ducts, the choking condition occurs with a higher outlet pressure. In other words, a much smaller inlet-to-outlet pressure ratio is needed to cause a choked flow. This highlights the danger of a partially blocked pore: since it only requires a small pressure ratio to choke the flow in the pore, this choked condition will not be detected from the macroscopic theory!
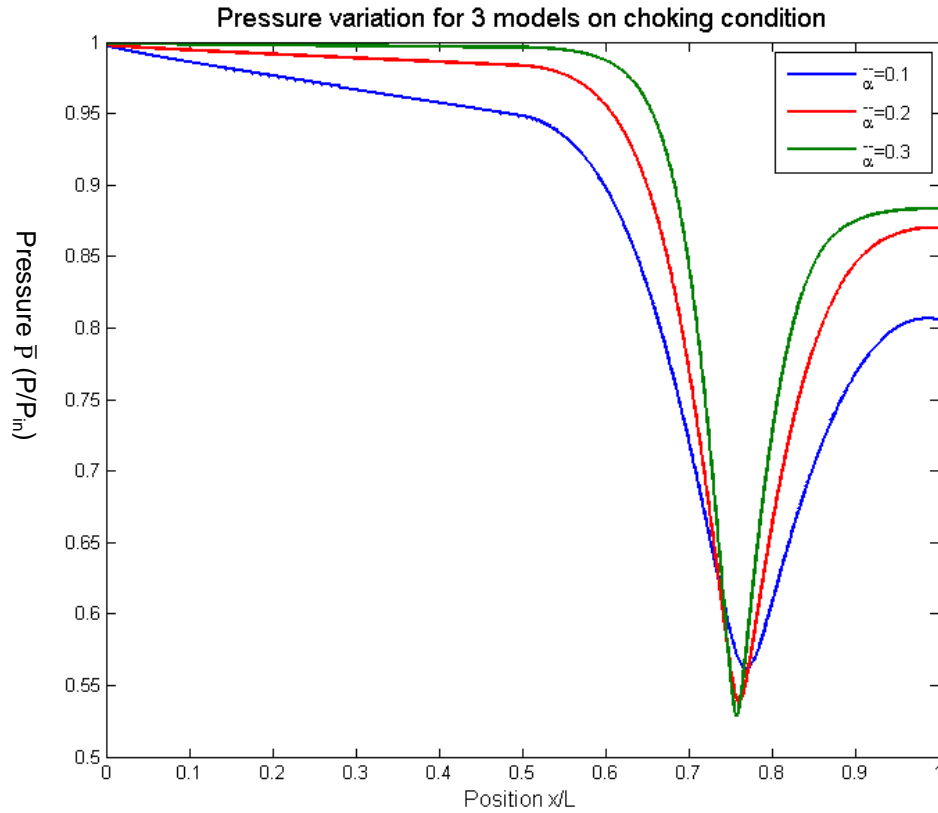
Fig 3.15 Pressure variation for 3 models on choking condition

The same simulations are performed with length of the duct ranging from $\bar{L} = 200$ to $\bar{L} = 600$. When one bump, the variation of the pressure ratio for different length and amplitude is shown in Fig. 3.16. It is concluded that for the same number of bumps, the longer the duct is, the higher the pressure ratio (P_{in}/P_{out}) is needed to reach the choking condition. For a fixed length, the bigger the bump amplitude, the lower the pressure ratio is needed to reach the choking condition.
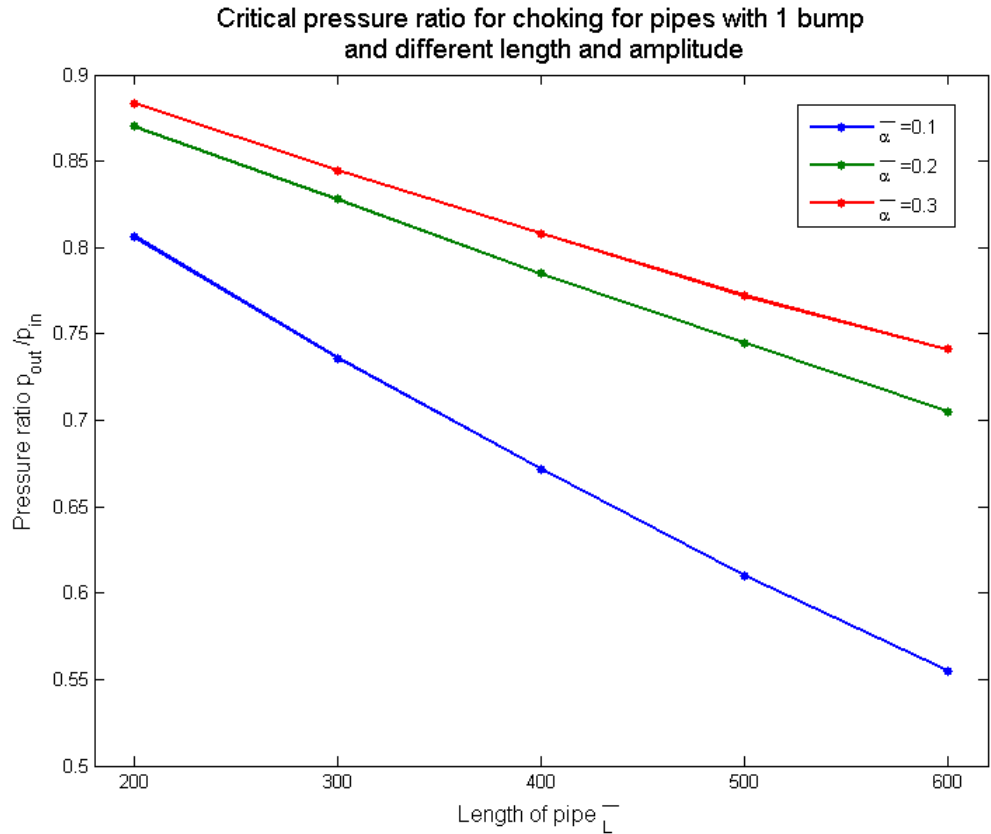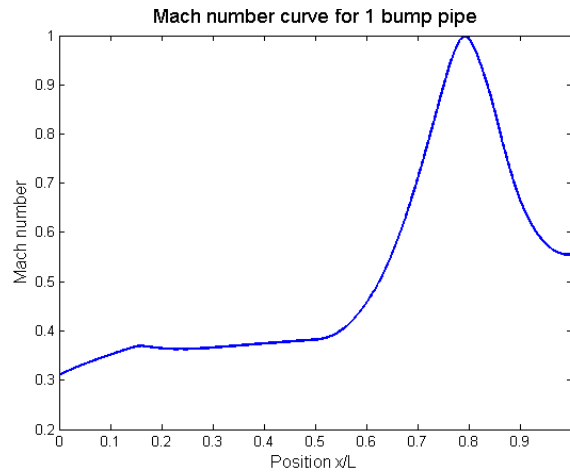
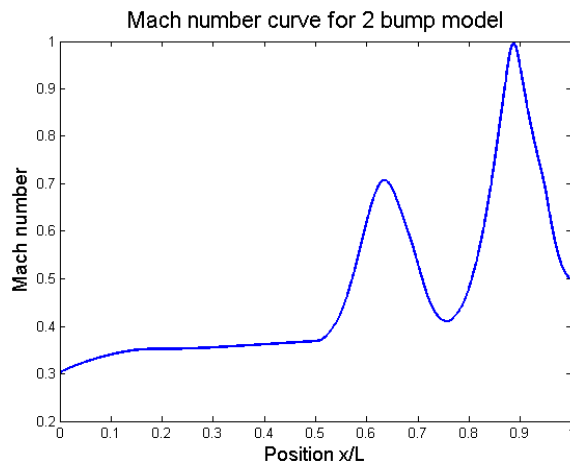Fig 3.16 Variation of the critical pressure ratio for choking for pipes with 1 bump and different length and amplitude.

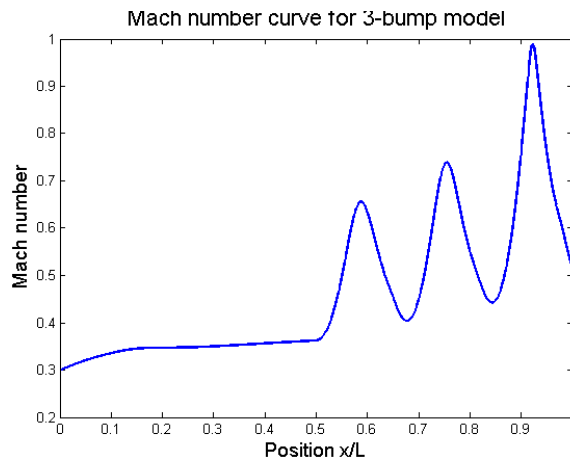The last factor to consider is the number of bumps. Simulations have been performed with 1 to 4 bumps for pipes with same length and same bump amplitude. The computed Mach number distribution along the duct with length of $\bar{L} = 500$ and amplitude of $\bar{\alpha} = 0.1$ are shown in Fig. 3.17 below.
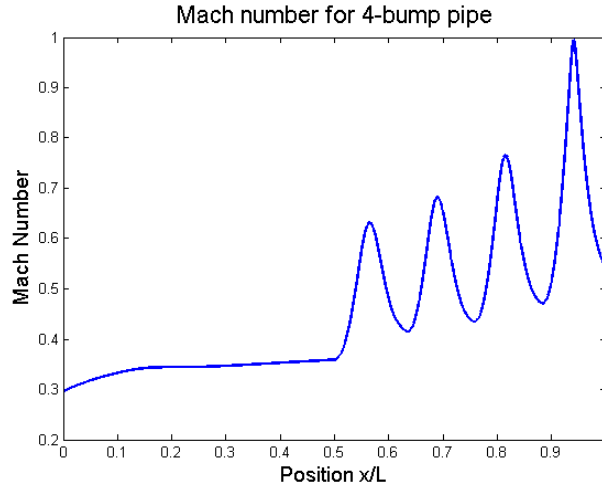
Mach number curve for 1 bump pipe

(a)

Mach number curve for 2 bump model

(b)

Mach number curve for 3-bump model

(c)

Mach number for 4-bump pipe

(d)

Fig 3.17 Mach number along the axis with (a) 1bump

(b) 2 bumps (c) 3 bumps (d) 4 bumps

From Fig. 3.17, it is seen that choking condition still all occur at the narrowest cross-section along the duct. For models with more than one bump, choking will first occur at the bump near the outlet.

Fig. 3.18 shows the variation of the critical pressure ratio (P_{out}/P_{in}) at choking condition for different lengths and number of bumps. In general, as the number of bumps increases, the critical pressure ratio P_{out}/P_{in} increases, indicative of a choking condition that is becoming easier to reach. However, as the number of bumps changed from 3 to 4, increase in this critical pressure ratio becomes very small. This is much more pronounced for shorter ducts, such as $\bar{L} = 200$ and $\bar{L} = 300$, where the change in the critical pressure ratio is nearly negligible.
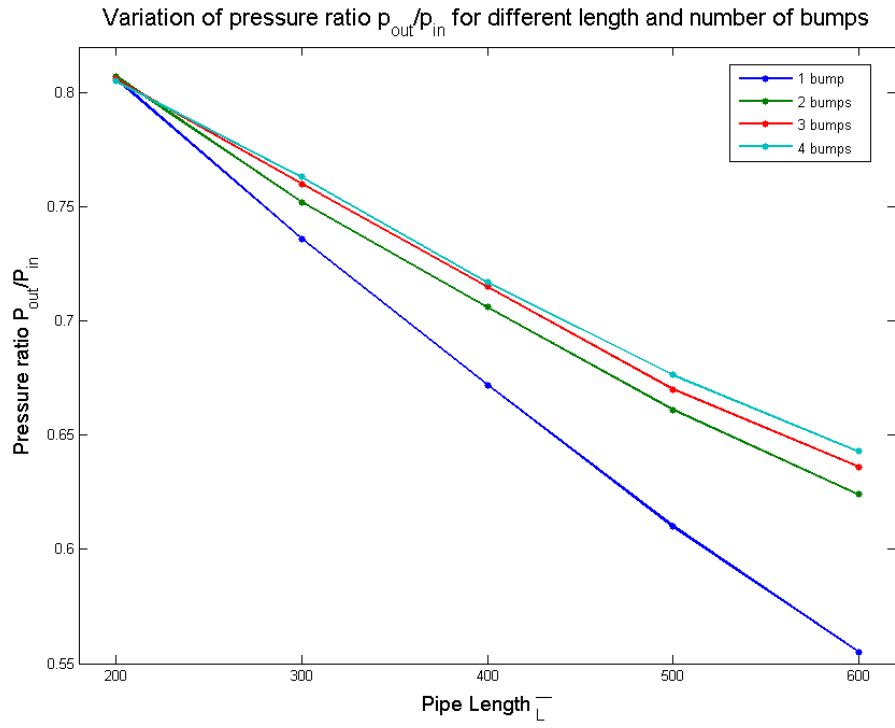
Fig 3.16 Variation of critical pressure ratio for choking with different number of

bumps and pipe lengths.

CHAPTER 4   CONCLUSION

As alluded to in the Introduction, choked flow is undesirable during petroleum production. The aim of the current thesis is to provide some guidance to avoid such choking condition from a pore-level analysis of the porous media flow. Our basic model is a compressible gas flow in a single microscopic pore with varicose cross-section. Our study shows that with one bump, choking condition will occur at the point of minimum flow area. With more than one bump, choking condition will occur at the narrowest point of the bump closest to the duct outlet. Choking condition will be easier to reach with a decreasing pressure ratio (P_{out}/P_{in}), since decreasing pressure ratio raises the mass flow-rate. The only way to avoid choking condition is to produce fluid at a pressure ratio larger than the critical pressure ratio for choking.

In our investigation, the length of the pore, the amplitude of the bump and the number of bumps are considered as three major factors affecting the choking condition. With the other factors remain the same, as the length of pore increases, the critical pressure ratio P_{out}/P_{in} required for choking decreased almost linearly. This shows that for shorter pores, a larger outlet pressure or well flowing pressure) is required to prevent choking. In the case of a fractured-well, this means that longer fractures are preferred.

Bump amplitude is also a significant factor on the choking condition. A larger amplitude increases the risk of a pore getting choked. In the case of a propped fracture, this suggests that use of smaller sand particles.

In general, increasing the number of bumps increase the possibility of choking. The relationship between the number of bumps and the critical pressure ratio P_{out}/P_{in} does not change linearly with the number of bumps used. The critical pressure ratio doesn't

change much as the number of bumps becomes large. Compared with the effect of the number of bumps, bump amplitude plays a more significant role affecting the critical pressure ratio for choking.

The study indicates that for a propped fracture, longer fractures and smaller size of sand particle will be effective for preventing choking.

REFERENCES

[1] Dake, L. P., 1978, Fundamentals of Reservoir Engineering, Elsevier, Amsterdam.

[2] Nind, T. E. W., 1989, Hydrocarbon Reservoir and Well Performance, Chapman and Hall, London.

[3] Fjaer, E., Holt, R. M., Horsrud, P., Raaen, A. M., and Risnes, R., 2008, Petroleum Related Rock Mechanics, Elsevier, Amsterdam.

[4] Bear, J., 1972, Dynamics of Fluids in Porous Media, Dover Publications, New York.

[5] Shreeve, R. P., 1968, "Supersonic Flow from a Porous Metal Plate," AIAA J., 6, pp. 752–753.

[6] Emanuel, G., and Jones, J. P., 1968, "Compressible Flow through a Porous Plate," Int. J. Heat Mass Transfer, 11, pp. 827–836.

[7] Nield, D. A., 1994, "Modeling High Speed Flow of a Compressible Fluid in a Saturated Porous Medium," Transp. Porous Media, 14, pp. 85–88.

[8] de Ville, A., 1996, "On the Properties of Compressible Gas Flow in a Porous Media," Transp. Porous Media, 22, pp. 287–306.

[9] Yan, J., Chen, K. P., Chen, M., Grapsas, N., and Zhang, F. X., 2011, "Short-Time Pressure Response during the Start-Up of a Constant-Rate Production of a High Pressure Gas Well," Phys. Fluids, 23, p. 043101.

[10] Donald A. Nield and Adrian Bejan. Convection in Porous Media. Springer, 2006.

[11] Jacob Bear, Dynamics of Fluids in Porous Media, Elsevier, 1972

[12] Constien, V. G.; King, M. T. 1985, Hydraulic fracturing process and compositions.

[13] Brad A. Meyer, Darrell W. Smith, Flow through porous media: comparison of consolidated and unconsolidated materials. American Chemical Society, 1985

[14] Green, L. & Duwez, P. 1951 Fluid flow through porous metals. J. Appl. Mech. 18, 39-45.

[15] Shreeve, R. P. 1968 Supersonic flow from a porous metal plate. AIAA Journal, 6, 752-753.

[16] Emanuel, G. & Jones, J. P. 1968 Compressible flow through a porous plate. Int. J. Heat Mass Transfer, 11, 827-836.

[17] Beavers, G. S. & Sparrow, E. M. 1971 Compressible gas flow through a porous material. Int. J. Heat Mass Transfer, 14, 1855-1859.

[18] Kodres, C. A. 1994 Flow parameter approach to modeling the flow of heated gases through high resistance porous media. Transport in Porous Media, 15, 229-249.

[19] Nield, D. A. 199.1 The limitations of the Brinkman-Forchheimer equation in modeling flow in a saturated porous medium and at an interface. Int. J. Heat and Fluid flow, 12, 269-272.

[20] Nield, D. A. 1994 Modeling high speed flow of a compressible fluid in a saturated porous medium. Transport in Porous Media, 14, 85-88.

[21] Nield, D. A. & Joseph, D. D. 1985 Effects of quadratic drag on convection in a saturated porous media. Phys. Fluids, 28(3), 995-997.

[22] de Ville, A. 1996 On the properties of compressible gas flow in a porous media. Transport in Porous Media, 22, 287-306.

[23] Levy, A., Sorek, S., Ben-Dor, G. & Bear J. 1995 Evolution of the balance equations in saturated thermoelastic porous media following abrupt simultaneous changes in pressure and temperature. Transport in Porous Media, 21, 241-268.

[24] Ciarletta, M. & Straughan, B. 2006 Poroacoustic acceleration waves. Proc. Roy. Soc. London A, 462, 3493-3499.

[25] Straughan, B. 2008 Stability and Wave Motion in Porous Media. Springer, New York.

[26] Jin, Yan. Chen, Kang Ping & Chen, Mian 2011 Development of tensile stress near a wellbore in high pressure gas flows. Intl. J. Rock Mech & Mining Sci. 48, 1313-1319.

[27] Chen, K. P. 2011 A new mechanistic model for prediction of instantaneous coal outbursts. Intl. J. Coal Geology, 87, 72-79.

[28] Jin, Yan. Chen, Kang Ping, Chen, Mian, Grapsas, Nicholas, 2012 Gas expansion induced acceleration effect in high pressure gas flows near a wellbore. J. Porous Media, 15(4): 317-328.

[29] Jin, Yan, Chen, Kang Ping & Chen, Mian, 2012 Highly compressible porous media flow near a wellbore: effect of gas acceleration, J. Fluids Eng.- Trans ASME, 134(1), 011301.

[30] Morita N, Whitfill DL, Massie I, Knudsen TW. Realistic sand-production prediction: numerical approach. SPE Prod Eng 1989;4:15–24.

[31] Morita N, Whitfill DL, Fedde OP, Lovik TH. Parametric study of sand production prediction: analytical approach. SPE Prod Eng 1989;4:25–33.

[32] Santarelli FJ. Similarities and differences between wellbore stability and sand production. In: Aasen JO, Berg E, Buller AT, Hjelmeland O, Holt RM, Kleppe J, Torsæter O, editors. Proceedings of the 3rd North Sea oil and gas conference, Trondheim, 30 Nov–2 Dec 1992. Berlin: Springer; 1994. p. 331–8.

[33] Fjaer E, Holt RM, Horsrud P, Raaen AM, Risnes R. Petroleum related rock mechanics.2nd ed. Amsterdam: Elsevier; 2008.

[34] Lambe TW, Whitman RV. Soil mechanics. New York: Wiley; 1991.

[35] Michel A. Saad, Compressible Fluid Flow Second Edition, 1993, Prentice Hall Publications.

[36] Ekachai Juntasaro, Putchong Uthayopas, Boonlue Sawatmongkhon and Khongthep Boonmee. High Performance computing for compressible turbulent flow. NECTEC Technical Journal, Vol. II, No. 9 P. 182-192

[37] ANSYS Inc, Ansys Fluent User's Guide, 2011

[38] ANSYS Inc, Ansys Fluent Theory Guide, 2009